Angular momentum gated giant dipole resonance measurements in the reaction ^{28}Si+^{58}Ni at $E(^{28}\mathrm{Si})=100$ and 125 MeV

S. K. Rathi,[1] D. R. Chakrabarty,[1] V. M. Datar,[1] Suresh Kumar,[1] E. T. Mirgule,[1] A. Mitra,[1] V. Nanal,[2] and H. H. Oza[1]
[1]*Nuclear Physics Division, Bhabha Atomic Research Centre, Mumbai 400 085, India*
[2]*Tata Institute of Fundamental Research, Mumbai 400 005, India*
(Received 1 October 2002; published 5 February 2003)

High-energy γ rays in the energy range of $\sim 4-35$ MeV were measured in coincidence with a γ-ray multiplicity detector array in the reaction ^{28}Si+^{58}Ni at $E(^{28}\mathrm{Si})=100$ and 125 MeV. The data were analyzed using the statistical model, and the giant dipole resonance parameters were extracted for various multiplicity windows. The exclusive temperature dependence of the γ-ray strength function has been obtained for a wide range of angular momentum, while the angular momentum dependence has been derived over a restricted range of temperature. The observed increase in the resonance width can be attributed to an increase in temperature. No dependence on angular momentum is observed. The last observation is at variance with the results in the tin region for similar rotational frequencies.

DOI: 10.1103/PhysRevC.67.024603 PACS number(s): 24.30.Cz, 25.70.Gh, 27.50.+e

I. INTRODUCTION

The giant dipole resonance (GDR) built on the excited states of nuclei [1,2] has been studied through high-energy γ-ray measurements in order to obtain information on nuclear properties at nonzero temperature and high angular momentum [3,4]. An important issue in these studies is the damping of the resonance as a function of angular momentum ($J\hbar$) and temperature (T). Some of the theoretical models for the T and J dependence of the GDR strength function, characterized by the resonance energy and width, are the collisional damping model [5,6], the phonon damping model [7], and the thermal fluctuation model [8–11]. The mixing of the correlated one particle one hole states, which constitute the GDR, with more complicated states lying at the same excitation energy is termed as collisional damping. The collisional damping model, which has been widely used in describing the GDR width at $T=0$, predicts a weak dependence of the width on T. The experimental data, on the other hand, shows a much stronger dependence and suggests some finite temperature effect which is not included in this model. The phonon damping model emphasizes the importance of the coupling of the GDR phonon to particle-particle and hole-hole configurations and seems to be in better agreement with the data. The thermal fluctuation model is the most widely used model. It incorporates the fluctuation in nuclear shape at finite temperature and the coupling of the GDR to nuclear quadrupole deformation leading to a splitting in the strength function. The observed width is then due to an averaging over an ensemble of nuclear shapes weighted by the appropriate Boltzmann factor. This model generally describes the experimental observations.

A systematic experimental measurement disentangling the effect of T and J on the GDR strength function is a challenging problem. Exclusive data from such measurements will help in improving our theoretical understanding of this fundamental excitation mode at finite temperature and angular momentum. Most of the measurements on the GDR on excited states have been made using heavy ion fusion reactions. The other method [12,13] is the measurement of high-energy γ rays in coincidence with the inelastically scattered ions populating the target nucleus at low J. The heavy ion fusion reactions populate nuclei over a wide range of excitation energy E_X and J. However, the increase in E_X with beam energy corresponding to a higher T, is accompanied by an increase in J. One way of disentangling the T and J dependence is by making measurements of high-energy γ rays in coincidence with the multiplicity of low-energy yrast γ rays, the latter providing a measure of J.

The increase of GDR width (Γ_{D}) with temperature is a well established experimental fact [3,4]. The main results of the multiplicity gated measurements extracting the J dependence [14–21] can be listed as follows. In $^{106-110}$Sn, Γ_{D} is reported to be roughly constant for J less than 30 and to increase by about 4.5 MeV at higher J up to 54 [14,15]. The average temperatures in these measurements, however, is not constant and ranges over 1.4 to 1.8 MeV. In ^{147}Eu, Γ_{D} is found to have a much weaker dependence changing by about 1 MeV over a range of $J\sim 35-50$ [18]. The average temperature in this measurement varies from 1.2 to 1.4 MeV. In the Dy and Er isotopes of similar mass, a stronger dependence of Γ_{D}, changing by about 6 MeV over a similar change in J, has been reported [16,17]. In the heavier nuclei ^{176}W [19] and ^{194}Hg [20], the observed Γ_{D} is almost independent of J in the range of 36–55 and 20–38, respectively. From the results reported for ^{197}Tl [21], one can draw a similar conclusion for angular momentum up to $\sim 32\hbar$. The variation in temperature in the measurements on heavier nuclei is much smaller. Translating the dependence on J to that on the rotational frequency (ω_{rot}), the above results on the variation of Γ_{D} can be interpreted as due to a systematic effect of ω_{rot} inducing nuclear deformation. However, the results on Dy and Er isotopes deviate from this trend showing a considerable effect also at somewhat lower frequencies. In Sn isotopes, the induced deformation is of oblate nature [15] at high ω_{rot}. Finally, whereas Γ_{D} has a significant dependence

TABLE I. Experimental parameters in the $^{28}Si+^{58}Ni$ reaction at two different beam energies. The fusion cross sections (σ_{fus}) are from the CASCADE code.

E_{beam} (MeV)	σ_{fus} (mb)	E_X^C (MeV)	J_0
100	523	49	30
125	938	66	46

on T and J, the centroid energy (E_D) appears to be almost independent of these two parameters in all these measurements.

In view of the necessity of such systematic measurements over a wider range of mass, temperature, and angular momentum, or rotational frequency, we have performed a multiplicity gated measurement of high-energy γ rays in a lighter mass region of $A\sim 85$. The heavy ion fusion reaction $^{28}Si+^{58}Ni$ was used to populate the compound nucleus ^{86}Mo. By performing the measurements at two beam energies, we have studied the GDR built on excited states with an average temperature of $\sim 1.1-1.6$ MeV and an average angular momentum ranging up to $\sim 31\hbar$. The rotational frequency range covered in this work is beyond those for the heavier nuclei mentioned above and has a good overlap with that in the Sn isotopes. It should also be noted that the proton rich nuclei contributing to the GDR γ production in this experiment, are mostly deformed in their ground states [22]. It is interesting to study their shape evolution at higher T and J.

II. EXPERIMENTAL METHOD

The experiment was performed by bombarding a self-supporting, rolled ^{58}Ni (99.9% enriched) target of thickness 0.5 mg/cm^2 with a collimated ^{28}Si beam from the 14UD BARC-TIFR Pelletron at Mumbai. The reaction was studied at two beam energies of 100 and 125 MeV. Table I lists the average excitation energies E_X^C and ''maximum'' angular momenta J_0 (defined later) in the compound nucleus ^{86}Mo at the two beam energies. High-energy γ rays were detected in an array of seven closely packed BaF_2 detectors [23], each 20 cm long and having a regular hexagonal cross section with a distance of 6 cm between the opposite edges. The front faces of the detectors were covered with a 5 mm thick lead sheet to cut down the low-energy γ rays and x rays. Cosmic ray events were reduced with the help of active plastic and passive lead shielding. The annular plastic detector surrounding the BaF_2 detectors had a length of 40 cm and thickness of 5 cm. The lead shield was 10 cm thick and placed on top and two sides of the plastic-BaF_2 assembly. The neutron and γ-ray backgrounds from the tantalum beam collimator were shielded by paraffin and lead, respectively. The detector assembly was kept at a distance of ~ 42 cm from the target and at an angle of 125° with respect to the beam direction. At 100-MeV beam energy the spectra were also measured at 45° and 90°.

The anode signal from the photomultiplier tube (PMT) of each detector was split into two paths. In one path, the signal was amplified using a fast amplifier with a variable gain. The gain matched signals from all the seven detectors were summed using a passive network and sent to two charge sensitive analog to digital converters (QDC). In the other path, the signal was amplified and fed to a constant fraction discriminator (CFD). The CFD outputs were time matched and the logical OR signal from all the seven CFDs was used to generate a short gate of 200 ns and a long gate of 2 μs duration for the two QDCs mentioned above. The outputs of the two QDCs were recorded event by event. The energy information was obtained from the QDC with the wider gate, the typical range being ~ 4 to 35 MeV. The ratio of the outputs of the QDCs was used to reject the pile-up events. The OR signal was also used in the time of flight (TOF) measurement in order to discriminate between γ rays and neutrons.

The multiplicity detector assembly consisted of 14 bismuth germanate (BGO) detectors, each 6.3 cm thick and having a regular hexagonal cross section with a distance of 5.6 cm between its opposite edges. They were close packed in two groups of seven each and placed above and below the target. The front face of each group was at a distance of about 2 cm from the target. The middle detector in each group was placed at a larger distance of about 5 cm to equalize the efficiency of all the detectors. The efficiencies were measured for 662 keV γ rays with a ^{137}Cs source kept at the target position. The total efficiency was $\sim 58\%$ and $\sim 68\%$ for the 100 MeV beam energy in two different experimental runs and $\sim 68\%$ for the 125 MeV beam energy. An analog signal was generated with an amplitude proportional to the number (fold) of BGO detectors producing simultaneous (within ~ 50 ns) outputs in each event. The CFD signal for each detector was generated with a threshold of ~ 100 keV. The OR of the CFD signals from the 14 BGO detectors (after time matching) was used as a trigger for the TOF measurement. Typical TOF spectra for two different γ energy windows in the BaF_2 array are shown in Fig. 1. The typical time resolution of ~ 3 ns was mainly arising from that of the BGO detectors, some misalignment in the time matching and the residual energy dependent walk in the CFDs. The separation of the gamma and neutron events are clearly visible in the figure.

The spectra of the pile-up (PU) parameter, defined as the ratio of the charges collected in the two QDCs and multiplied by a suitable constant, are shown in Fig. 2 for two different energy windows. The spectra shown are generated by putting the prompt γ gate on the TOF spectra. The portions of the spectra outside the peak regions in Fig. 2 correspond to events with pile up and were rejected in the off-line data analysis.

The energy calibration of the BaF_2 detector assembly was done by using the ^{241}Am-^{9}Be (4.43 MeV) and ^{238}Pu-^{13}C (6.13 MeV) radioactive sources. The 15.1 MeV γ ray from the reaction $^{12}C(p,p')^{12}C$ at $E_p\sim 19.6$ MeV was used as the high-energy calibration point. At the high voltage applied to the PMTs, the linearity has been checked [23] up to ~ 35 MeV. The gain variation of the detectors was monitored at regular intervals of 2–3 h, using the 4.43 MeV and 6.13 MeV lines and the γ spectra in each run was corrected for accordingly. The typical variation in gain over this period

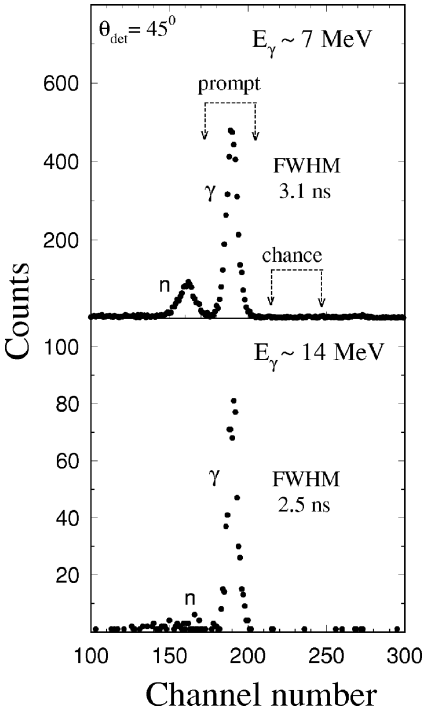

FIG. 1. Examples of TOF spectra with fold $F>3$ and energy around 7 and 14 MeV in the BaF_2 detector. Neutron and γ peaks are shown. Prompt and chance windows used in the off-line analysis are also indicated.

was $<1\%$. The beam charges collected in the experiment were 1 and 0.25 particle millicoulomb (pmC) for two different runs at 100 MeV beam energy and 0.8 pmC at 125 MeV beam energy.

The background in the γ spectra was expected to be mainly from oxygen and carbon impurities in the ^{58}Ni target. The oxygen impurity was due to the partial oxidation of the targets, whereas the carbon impurity was generated on the surface from the beam bombardment over a long time. In order to estimate the contributions from these impurities the following measurements were also made. Targets of carbon ($\sim 50\ \mu g/cm^2$) and oxygen (WO_3, $\sim 150\ \mu g/cm^2$) were bombarded with ^{28}Si beam of 100 and 125 MeV and the γ spectra were measured. These were then multiplied by the relative abundances of carbon and oxygen in the ^{58}Ni target to that in the C and WO_3 targets. These relative abundances were obtained from the yields of characteristic α groups from the reactions $^{12}C(^{12}C,\alpha)$ and $^{16}O(^{12}C,\alpha)$ feeding discrete states in ^{20}Ne and ^{24}Mg, respectively. These measurements were made with a ^{12}C beam of energy 35 MeV, and α particles were detected in a surface barrier detector (2 mm thick) placed at $\sim 15°$ with respect to the beam direction. In order to correct for the resonance effect in the yield of these α groups, these data were taken over a beam energy range, spanning the energy loss in the target.

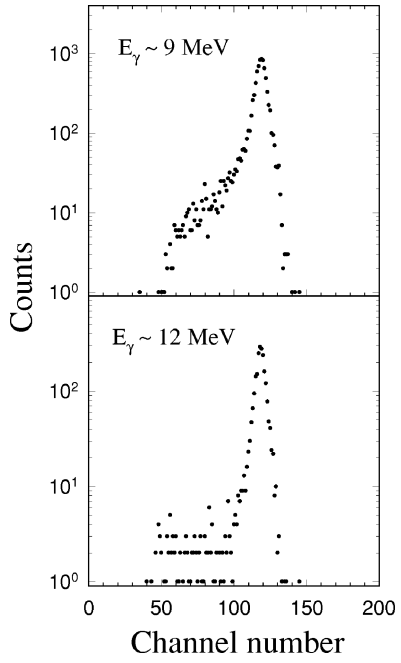

FIG. 2. Examples of the spectra of pile-up parameter (see text) for energy around 9 MeV and 12 MeV in the BaF_2 detector.

III. EXPERIMENTAL DATA ANALYSIS

The high-energy γ spectra were extracted from the off-line analysis of the data, recorded in the event by event mode, after putting proper cuts on the TOF and the PU parameter. The spectra were generated for various folds and for each combination of the beam energy and target. The contribution due to the chance coincidence events within the prompt γ window in the TOF spectrum was subtracted. Similarly, the contribution due to the pile-up events under the peak in the PU spectrum was corrected from an extrapolation of the pile-up tail under the peak region.

The background in the γ spectra arising from the carbon and oxygen impurities in the main target was estimated as discussed earlier. Figure 3 shows some examples of the γ spectra from the main target along with the estimated impurity contribution. These were subtracted from the measured spectra for various folds. The contribution decreases with increase in fold, the maximum being up to 12% for fold $F=1$.

A residual cosmic ray background survived in spite of the passive and active shielding of the detector, as indicated by the flat part of the spectra (Fig. 3) beyond ~ 25 MeV. This background, which also decreases with fold, was removed by subtracting the average yield in the region of ~ 25–35 MeV.

The fold distributions were created for different energy windows in the BaF_2 detector, from the high-energy γ spectra obtained for each fold. These distributions are shown in Fig. 4 for some E_γ windows. These data at 100 MeV beam energy are for the BGO efficiency of 58%. The fold distributions are different for different γ energy windows. In order to obtain the multiplicity (M_γ) distribution corresponding to these fold distributions, first, the fold response of the BGO-multiplicity array was calculated for different discrete M_γ with a Monte Carlo computer program. The convolution of the input M_γ distribution with these response functions is then compared with the experimental data.

A one-component Gaussian M_γ distribution with a mean

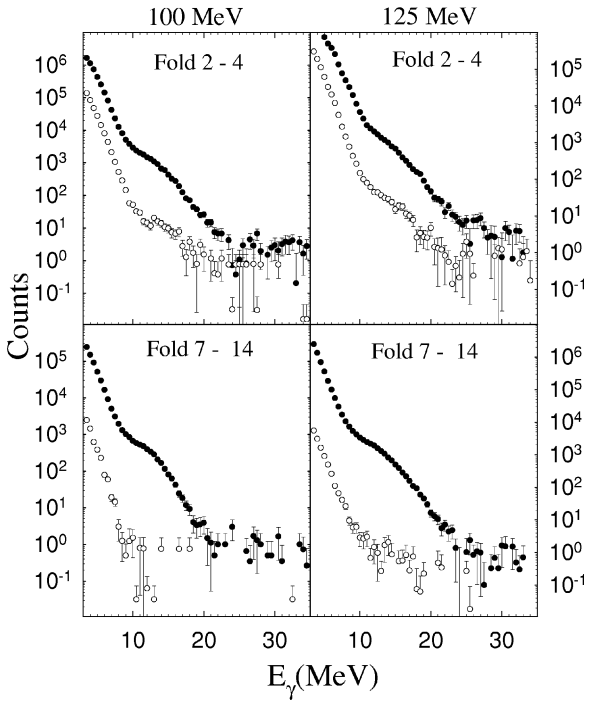

FIG. 3. Examples of γ-ray spectra at $\theta = 125°$ in the reaction ^{28}Si+^{58}Ni (filled circles) and background from carbon and oxygen impurities (open circles) at two different beam energies and fold windows.

of 7–9 and full width at half maximum (FWHM) $\sim$11, could fit the data for E_γ above 12 MeV. On the other hand, a second low multiplicity component, with a mean of 0–4 and FWHM$\sim$5, had to be added for lower E_γ. The relative intensity of this component peaks at around 8 MeV and falls on either side becoming negligible beyond $\sim$12 MeV. While we do not understand quantitatively the origin of this second component, this should be due to nonfusion events in the target. The fold distributions from fusion events are expected to be essentially similar for various γ energy windows. This conjecture was checked in a separate experiment at 100 MeV beam energy by making the measurements in coincidence with characteristic γ rays from evaporation residues. The BGO efficiency in this run was $\sim$62%. Figure 5 shows the fold distributions in singles and in coincidence with four γ transitions in the residue nuclei ^{83}Y and ^{80}Sr. The γ rays were detected in high purity germanium clover detectors. The coincident fold distributions are seen to be similar for various γ ray energy windows in marked contrast to the single distributions. From the best fits of the fold distributions, shown in Fig. 4, the contributions from the second component were estimated for each fold. These were subtracted in order to derive the γ spectra from pure fusion events. The uncertainty in this procedure, arising from the range of acceptable parameters for the second component, was included in the derived spectra. Figure 6 shows some examples of the corrected and the uncorrected spectra for different fold windows. The correction, as expected, decreased as a function of fold and became insignificant for fold $F > 4$.

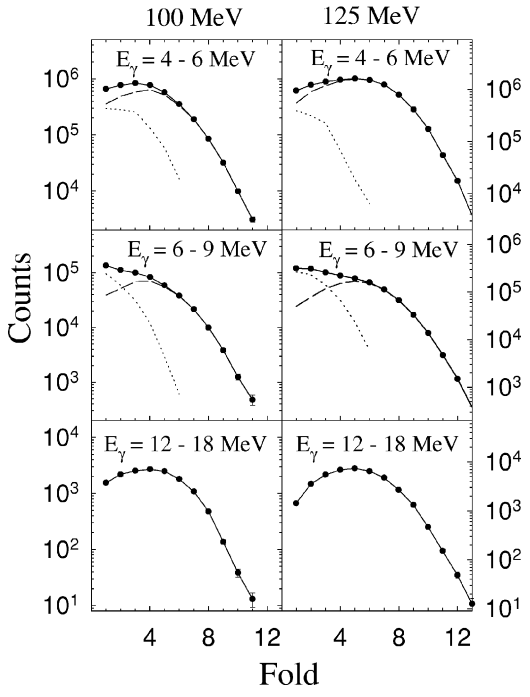

FIG. 4. Experimental fold distributions and the best fits for various γ energy windows. The main component and the low multiplicity component are shown by dashed and dotted lines, respectively.

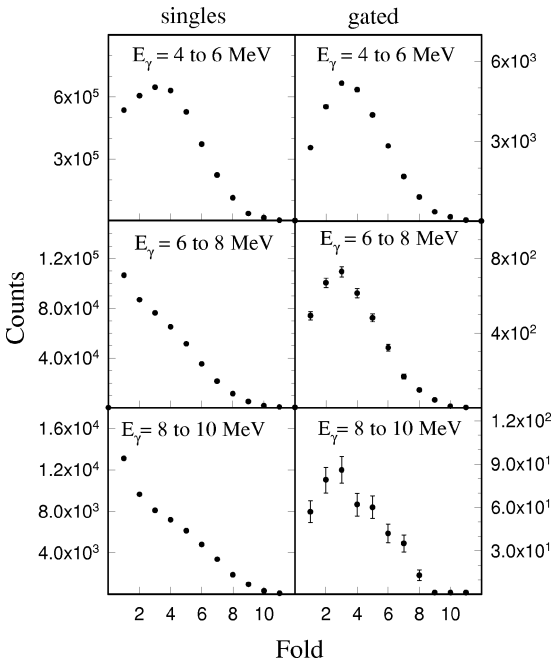

FIG. 5. Experimental fold distributions for various γ energy windows in singles and in coincidence with evaporation residue lines at 100 MeV.

In the final step, the Doppler correction was applied to the spectra at all angles by assuming the source velocity to be the compound nuclear recoil velocity. For 100 MeV beam energy the ratios of the Doppler corrected γ spectra at different angles (Fig. 7) show no discernible angular anisotropy. These spectra at the three angles were therefore added up to improve the statistics. Finally, the spectra were grouped into

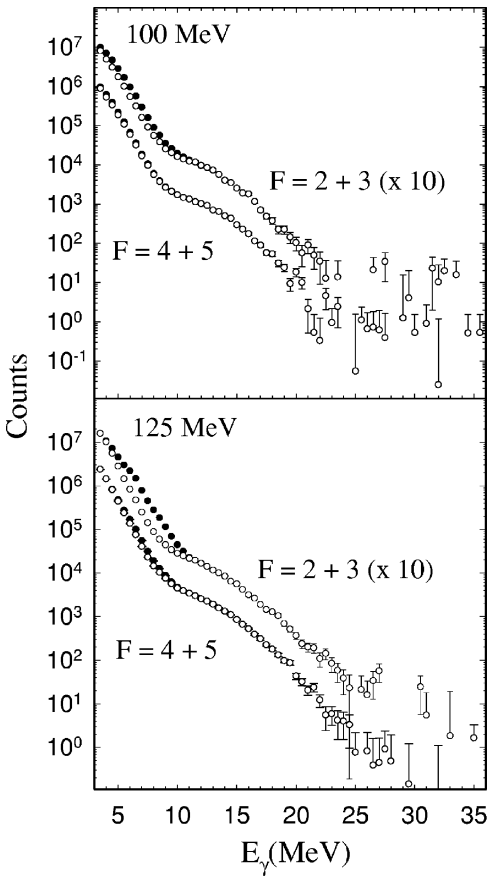

FIG. 6. Examples of γ-ray spectra before (filled circles) and after (open circles) correction for the nonfusion events for two-fold(F) windows.

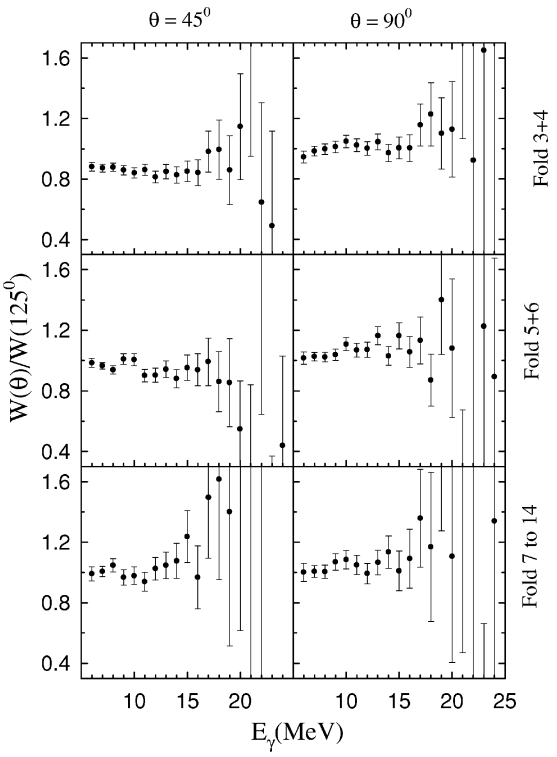

FIG. 7. Ratio of γ yields at 45° and 90° to that at 125° for various fold windows at 100 MeV.

different fold windows before comparing with the statistical model calculations discussed in the following section.

IV. STATISTICAL MODEL ANALYSIS

The statistical model analysis consists of extracting the GDR strength function, characterized by energy and width parameters, for various fold windows from a comparison with the statistical model calculations. The code CASCADE [24], with the necessary modifications, was used for this purpose. In these calculations the angular momentum distribution in the compound nucleus was assumed to have the form

$$\sigma(J_C)=\sigma_0\frac{(2J_C+1)}{1+\exp[(J_C-J_0)/\delta J]} \qquad (1)$$

with $\delta J=3$. The parameters J_0 and σ_0 were consistent with the total fusion cross sections listed in Table I. This full distribution, however, should not be used in the calculation of the γ spectra for different fold windows which correspond to different ranges of the compound nuclear angular momentum J_C. This is because the calculated γ spectrum for a given set of GDR parameters changes with J_C.

The appropriate J_C distribution for each fold window was derived by adopting the following procedure. First, the CASCADE calculation was done for each J_C using a fixed fusion cross section and the residue spin (J_R) distributions were obtained. The conversion of the J_R distribution to a fold (F) distribution was done by creating the J_R to F response function relevant for the present setup. This was obtained considering the following points. The residue spin state can lose an angular momentum of 2 or $1\hbar$ for every low-energy near-yrast γ transition. The relative probability of a $\Delta J=1$ transition was taken as a parameter. The energy of the γ rays are not constant and depends on the initial and final J in a given transition. Thus the energy dependence of the efficiency and the cross talk probabilities of the BGO setup should be considered. This information was obtained by running the electron gamma shower code EGS4 [25] for the BGO setup. Finally, each event is accompanied by the statistical γ rays of average energy E_S and multiplicity M_S. A Monte Carlo computer program was written incorporating all these aspects. All these parameters were obtained by fitting the measured γ energy gated F distributions as described below. From the fold distribution for each J_C thus calculated, a population matrix $\sigma(F,J_C)$ was created. By projecting this matrix onto the J_C axis, the compound nuclear spin distribution for different fold windows were finally obtained.

For fitting the experimental data on F-distributions, the γ energy gated distributions were calculated as follows. From the γ spectra and J_R distributions for each J_C, the relative probabilities (a) $P(E_\gamma,J_C)$ for different J_C yielding a certain E_γ and (b) $P(J_C,J_R)$ for different J_R originating from a certain J_C, were derived. The population of the different residue spins for a certain E_γ is then given by

$$\sigma(E_\gamma,J_R)=\sum_{J_C} P(E_\gamma,J_C)P(J_C,J_R)\sigma(J_C), \qquad (2)$$

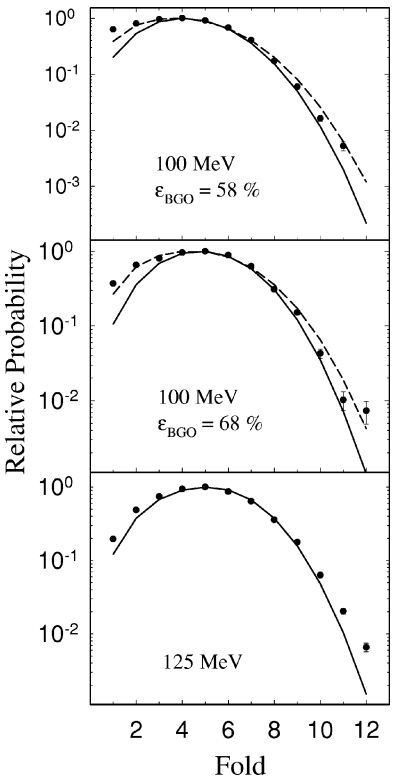

FIG. 8. Comparison of the experimental and calculated fold distributions for different data sets for $E_\gamma = 12-22$ MeV. The solid and dashed curves are discussed in the text.

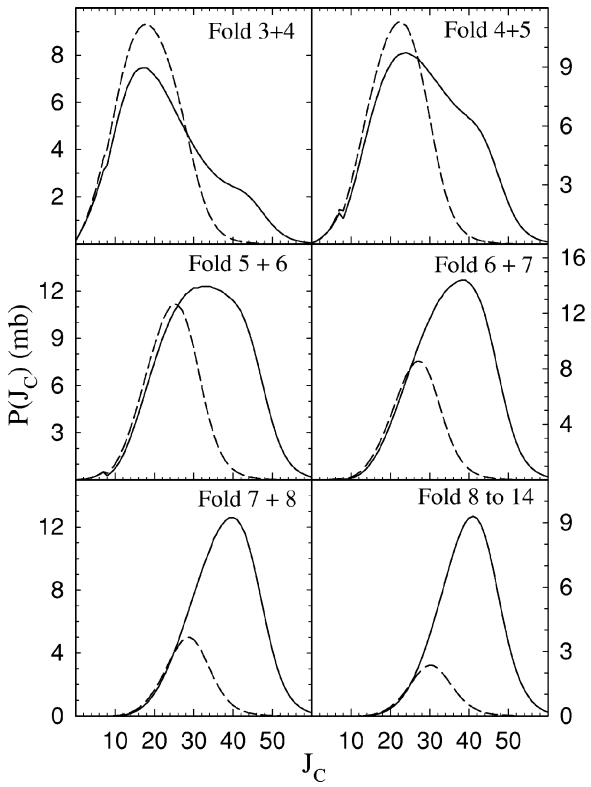

FIG. 9. Compound nucleus spin distribution for various fold windows for beam energies of 100 (dashed line) and 125 MeV (solid line).

where $\sigma(J_C)$ is the compound nuclear spin population given in Eq. (1). This expression assumes that the J_R distribution for a given J_C is independent of any γ-ray emission. This is not strictly correct. For the present system, the α particle emission, which takes away a higher angular momentum, is important particularly at high J_C. However, if a high-energy γ ray is emitted in the cascade, the average angular momentum loss will be less and the nucleus should land up in a higher residue spin. This effect, therefore, should be more, the higher the E_γ as well as J_C. The residue spin distribution $P(J_C, J_R)$ in Eq. (2) was therefore shifted by an amount $a_s E_\gamma J_C$, treating a_s as a parameter. The choice of this dependence was guided by simplicity and the value of a_s needed in the fit was consistent with the results of a Monte Carlo CASCADE [26] calculation. The fold distributions for the γ energy window at 12–22 MeV were calculated and all the parameters were adjusted to obtain a reasonable fit to the experimental data. These are shown in Fig. 8 (solid lines), in which the relative probability of $\Delta J = 1$ is between 0.05 and 0.15. The a_s parameter mentioned above is between 0.003 and 0.005. The statistical γ transition has an energy $E_S \sim 2.3$ MeV and M_S between 1.2 and 1.6. The E_S and M_S values are also supported by Monte Carlo calculations mentioned above. In Fig. 8, the calculations do not reproduce the $F = 1$ and 2 data points well for the 100 MeV beam energy. For this case another prescription of J_R to F conversion was also tried. The fold distribution for a given J_R was assumed to be a Gaussian with a mean $M = K + bJ_R$ and FWHM $= c + dJ_R^p$. The dashed lines in Fig. 8 show the calculated distributions with $K = 0.8$, $b = 0.6$, $c = 0$, $d = 0.018$, and $p = 1.8$. Folds 1 and 2 are better reproduced. However, the compound nuclear J distributions with this prescription are almost identical to those with the earlier ones and the derived GDR parameters, to be discussed later, agree well within the error bars. Figure 9 shows the compound nuclear J distributions that are used in the subsequent calculations for different fold windows.

The prescription for the nuclear level density (NLD) used above and in all subsequent calculations is that of Ignatyuk [27] as elaborated in Ref. [26] with the asymptotic (liquid drop) value for the NLD parameter fixed at $\tilde{a} = A/7.5$ MeV^{-1}. The J dependence of the moment of inertia is as given by the default prescription in CASCADE. The optical model potential parameters for the calculation of the transmission coefficient for neutron, proton, and α were taken from Refs. [28–30], respectively. These choices were guided by the measurement of proton and α particle spectra in this reaction at the same two beam energies [26].

The GDR strength function to be extracted from the analysis was parametrized as a one- or two-component Lorentzian given by

$$F_L(E_\gamma, E_R, \Gamma) = \frac{\Gamma^2 E_\gamma^2}{(E_\gamma^2 - E_R^2)^2 + \Gamma^2 E_\gamma^2}.$$

The effective transmission coefficient for γ decay competing with particle decay in a statistical evaporation can then be written as

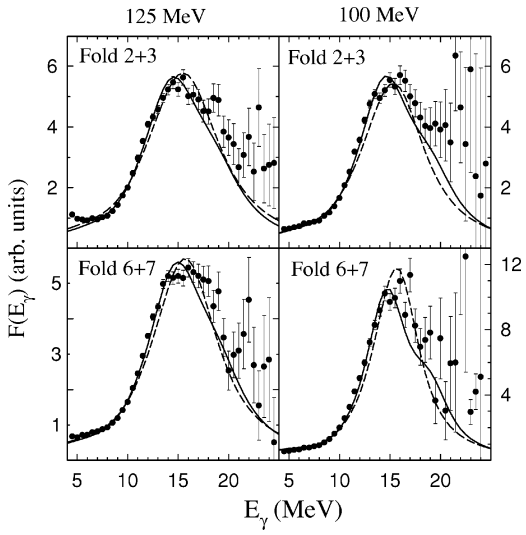

FIG. 10. Divided plots of the measured γ spectra and the best spherical (dashed line) and oblate (solid line) fits at 100 and 125 MeV.

$$T(E_\gamma)=C\frac{NZ}{A}E_\gamma^2\left[\frac{S_1F_L(E_\gamma,E_1,\Gamma_1)}{\Gamma_1}+\frac{S_2F_L(E_\gamma,E_2,\Gamma_2)}{\Gamma_2}\right]$$

with $C=20.9\times10^{-6}$ MeV^{-1}. Here $E_{1(2)}$ and $\Gamma_{1(2)}$ are the resonance energies and widths for the two components and $S_{1(2)}$ are the strengths. $S_1+S_2=1$ corresponds to the 100% exhaustion of the sum rule strength. $S_2/S_1=2$ and 1/2, respectively, denote the GDR in a prolate and an oblate deformed nucleus. A spherical nucleus corresponds to a one-component Lorentzian.

In the analysis, the GDR parameters were varied for the different assumptions of spherical, prolate, or oblate shapes. A sum rule strength of 100% was used in all the calculations. The calculated γ spectra were folded with the detector response function simulated using EGS4 [25], and were compared with the data for each fold window. For a sensitive comparison, both the data and the calculated spectra were converted to linearized divided plots of $F(E_\gamma)$ [31]. These plots were generated by dividing both the experimental and the calculated spectra by a statistical spectrum assuming a constant $E1$ strength. This was arbitrarily chosen to be 0.2 W.u. and the normalization to the data was done at $E_\gamma \sim 8$ MeV. The chi-square values for the fits were calculated for the E_γ range of 8–22 MeV encompassing the GDR bump in all the spectra.

V. RESULTS AND DISCUSSION

A one-component Lorentzian strength function cannot fit the data as shown in Fig. 10. Similarly, a two-component Lorentzian corresponding to an oblate shape fails under the assumption [9] that $\Gamma_2 \geqslant \Gamma_1$. The data can be best described by assuming a prolate shape as shown in Figs. 11–13. It may be mentioned that the absolute normalization in these fits is between $\sim$0.8 and 1.2. The best fit values of these parameters are listed in Table II. From these GDR parameters, the centroid E_D, defined as $(E_1+2E_2)/3$ and the width Γ_D,

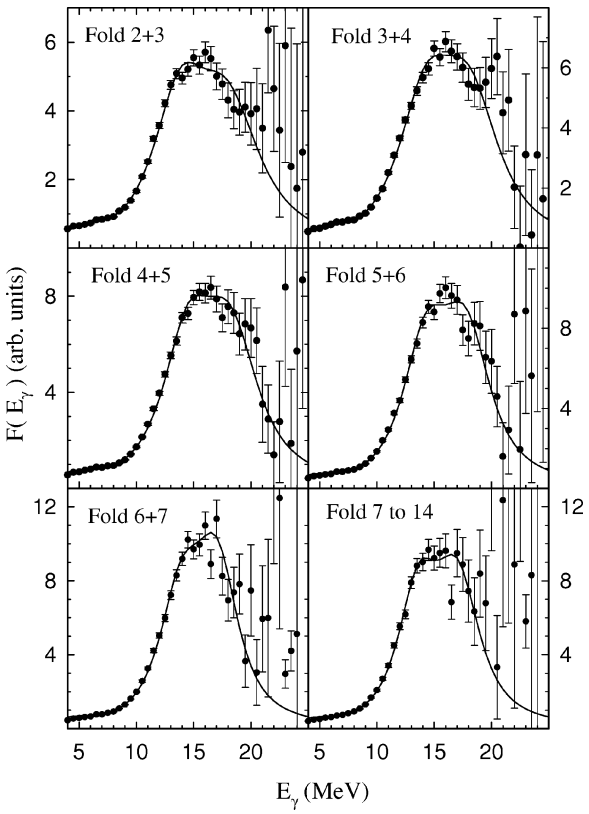

FIG. 11. Divided plots of the measured γ spectra and the best prolate fits at 100 MeV and BGO efficiency $\epsilon_{BGO}\sim58\%$.

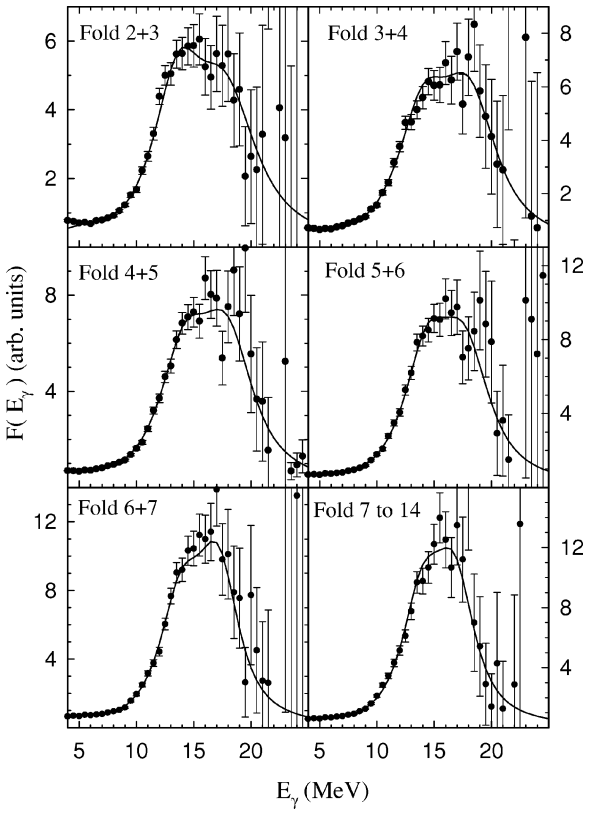

FIG. 12. Same as in Fig. 11 for $\epsilon_{BGO}\sim68\%$.

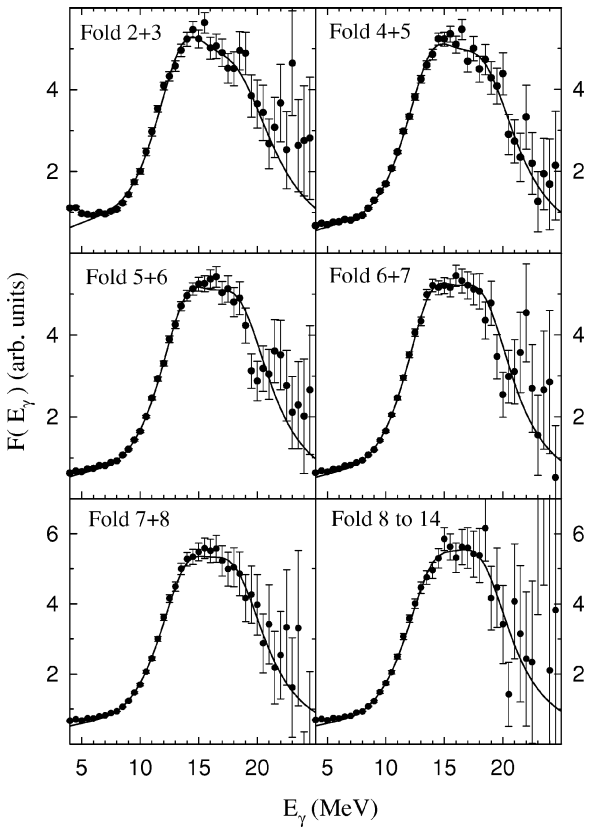

FIG. 13. Same as in Fig. 11 at 125 MeV and $\epsilon_{BGO}\sim 68\%$.

defined as the FWHM of the two-component strength function, are obtained. These are listed in Table III. The effective quadrupole deformation parameter β can be derived from the ratio of E_2 to E_1, utilizing the expression in Ref. [33], as

$$\beta = \sqrt{\frac{4\pi}{5}}\left(\frac{\delta - 1.0}{0.5\delta + 0.87}\right),$$

where $\delta = E_2/E_1$. These are also listed in Table III.

Figure 14 shows the extracted Γ_D and E_D values for different fold windows. The GDR width decreases significantly as a function of fold at 100 MeV. A similar trend is seen at 125 MeV, although the rate of decrease is not as prominent. The centroid energy is close to the ground state GDR value for the nuclei in this mass region [32].

In order to discuss the above results in terms of the effect of angular momentum and temperature, it is necessary to define the average values of these quantities for E_γ near the GDR centroid energy. Since the GDR emission takes place in different steps of decay and also for a range of J for any fold window, only the average values can be considered. The average temperature relevant for GDR decay is calculated by various authors following different procedures. The average J is often taken to be that of the initial compound nucleus. This is a valid approximation for heavy nuclei, which deexcites mainly through neutron emission carrying a small angular momentum, but is not justified for the lighter mass region. We have made detailed calculations to extract these values using the code CASCADE after the following modifi-

TABLE II. Best prolate fit GDR parameters for various fold windows from three data sets. Sets *A* and *B* correspond to $\epsilon_{\rm BGO}\sim 58\%$ and 68%, respectively, at 100 MeV. All energies are in MeV. The χ^2 is for 57 data points.

$E_{\rm beam}$	Fold	E_1	Γ_1	E_2	Γ_2	χ^2
	2+3	14.6±0.3	4.5±0.3	18.9±0.6	6.3±0.7	58
	3+4	15.0±0.3	4.5±0.3	18.9±0.5	5.7±0.5	72
100	4+5	15.2±0.3	4.0±0.3	19.0±0.5	5.2±0.5	65
(*A*)	5+6	14.9±0.3	3.5±0.3	18.5±0.4	4.4±0.4	73
	6+7	14.5±0.3	3.3±0.3	17.7±0.4	3.6±0.4	61
	7-14	14.2±0.3	3.0±0.3	17.7±0.5	3.9±0.5	59
	2+3	14.4±0.4	4.0±0.4	18.7±0.9	6.0±0.9	25
	3+4	14.8±0.4	4.2±0.4	18.9±0.8	5.1±0.7	29
100	4+5	14.9±0.4	4.0±0.4	18.7±0.5	4.8±0.6	37
(*B*)	5+6	15.0±0.4	3.5±0.4	18.4±0.5	4.5±0.6	27
	6+7	14.5±0.4	3.2±0.4	17.8±0.5	3.4±0.6	27
	7-14	14.5±0.4	2.9±0.4	17.4±0.5	3.4±0.6	36
	1+2	14.4±0.4	5.9±0.5	19.4±0.8	8.2±1.0	68
	2+3	14.6±0.3	5.3±0.4	19.4±0.8	7.8±0.8	49
	3+4	14.7±0.3	5.1±0.4	19.3±0.6	7.0±0.6	52
125	4+5	14.8±0.3	5.1±0.4	19.4±0.6	6.8±0.6	52
	5+6	14.8±0.3	5.0±0.4	19.4±0.6	6.4±0.6	37
	6+7	14.7±0.3	4.9±0.4	19.2±0.6	6.2±0.6	36
	7+8	14.7±0.4	5.0±0.4	19.0±0.6	6.3±0.8	24
	8-14	14.8±0.4	5.2±0.4	19.0±0.6	6.2±0.8	29

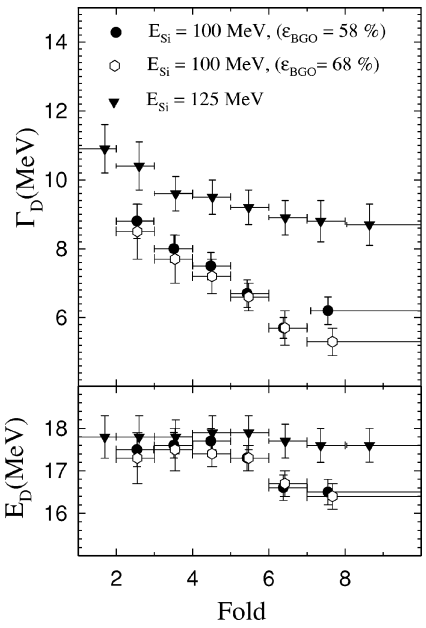

FIG. 14. GDR width and centroid energy extracted from CASCADE fits for various fold windows.

cations. At every step of γ decay for a given E_γ, the angular momentum J_f and the temperature T_f of the final state have been obtained. The former is straightforward and the latter is calculated as $U=aT_f^2$, where $U=E_{xf}-E_{rot}(J_f)-\Delta_P$. The rotational energy $E_{rot}(J_f)$ and the pairing energy Δ_P are subtracted from the final state energy E_{xf} and the level density parameter a is calculated at the corresponding U following the expression of Refs. [26,27]. The pairing energy is assumed to be independent of E_X and J. Two matrices of the cross section $\sigma(E_\gamma,T_f)$ and $\sigma(E_\gamma,J_f)$ are thus created. From these matrices, the T_f and J_f distributions for any γ-ray energy can be calculated. Finally, the average and the standard deviation (σ) of these distributions are derived. Table III lists these values for different fold windows and beam energies for $E_\gamma \sim 17$ MeV, which is the GDR centroid energy in the present case.

Figure 15 shows Γ_D and E_D as a function of average temperature. The increase in width with temperature is more prominent up to ~ 1.3 MeV. It may be noted that each point in the figure corresponds to a range of temperature which can be deduced from the σ values given in Table III. The inherent temperature dependence is, therefore, expected to be steeper for the lower temperature part. However, the basic trend of a monotonic increase will be similar. The other point to note is that at a given beam energy, the points in the figure at lower average T correspond to higher average J. A part of the observed width at high J should arise from the Coriolis splitting [8]. If this contribution is subtracted, the resultant dependence of Γ_D on T will be steeper.

The effective β parameters extracted from the present data are also shown in Fig. 15 as a function of T. There is a mild increase of deformation with T. However, it may be recalled that even at the highest angular momentum the nuclei do not show oblate shapes in contrast to the situation in the Sn region. The observed increase in effective β and Γ_D with T, in the present case, could arise from shape fluctuations.

TABLE III. Average angular momentum $\langle J\rangle$ and temperature $\langle T\rangle$ with corresponding standard deviations (σ), β parameter, E_D and Γ_D for various fold windows. Temperature and energies are in MeV. *A* and *B* are as defined in Table II.

E_{beam}	Fold	$\langle J\rangle$	σ_J	$\langle T\rangle$	σ_T	β	E_D	Γ_D
	2+3	12.4	6.0	1.28	0.27	0.31±0.05	17.5±0.4	8.8±0.5
	3+4	15.0	6.4	1.25	0.26	0.28±0.04	17.6±0.3	8.0±0.4
100	4+5	17.5	6.2	1.21	0.26	0.27±0.04	17.7±0.3	7.5±0.4
(*A*)	5+6	20.0	6.0	1.17	0.26	0.26±0.04	17.3±0.3	6.7±0.4
	6+7	22.0	5.5	1.13	0.26	0.24±0.04	16.6±0.3	5.7±0.3
	7-14	23.6	5.1	1.09	0.23	0.26±0.04	16.5±0.3	6.2±0.4
	2+3	10.8	5.5	1.30	0.27	0.31±0.06	17.3±0.6	8.5±0.8
	3+4	13.5	6.2	1.27	0.26	0.29±0.05	17.5±0.5	7.7±0.7
100	4+5	16.0	6.2	1.23	0.26	0.27±0.05	17.4±0.3	7.2±0.5
(*B*)	5+6	18.7	6.0	1.19	0.26	0.24±0.05	17.3±0.3	6.6±0.4
	6+7	20.9	5.5	1.15	0.26	0.24±0.05	16.7±0.3	5.7±0.4
	7-14	23.1	5.1	1.10	0.23	0.22±0.05	16.4±0.3	5.3±0.4
	1+2	10.6	6.0	1.60	0.34	0.36±0.06	17.8±0.5	10.9±0.7
	2+3	13.3	7.2	1.57	0.34	0.34±0.06	17.8±0.5	10.4±0.7
	3+4	16.8	8.1	1.53	0.34	0.33±0.05	17.8±0.4	9.6±0.5
125	4+5	20.6	8.5	1.47	0.34	0.32±0.05	17.9±0.4	9.5±0.5
	5+6	24.1	8.2	1.41	0.33	0.32±0.05	17.9±0.4	9.2±0.5
	6+7	26.9	7.7	1.36	0.31	0.32±0.05	17.7±0.4	8.9±0.5
	7+8	29.2	7.3	1.31	0.31	0.31±0.05	17.6±0.4	8.8±0.6
	8-14	31.2	6.8	1.26	0.30	0.30±0.06	17.6±0.4	8.7±0.6

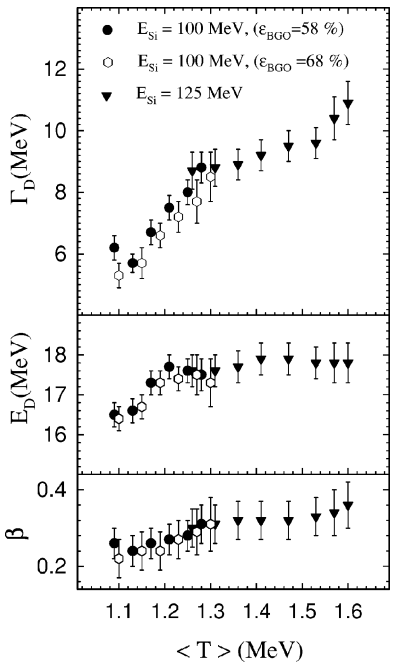

FIG. 15. GDR width, centroid energy, and deformation parameter as a function of average *T*. See Table III for the spread in *T* for each data point.

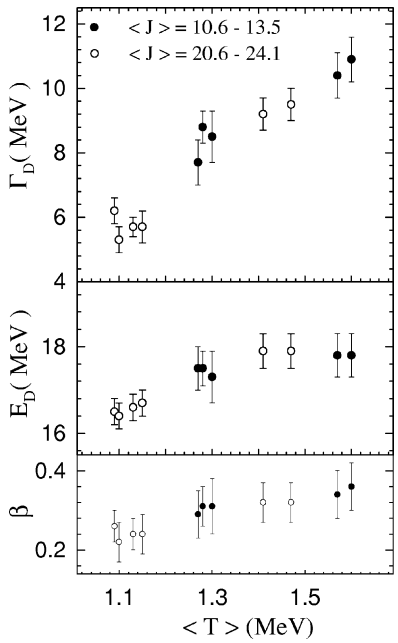

FIG. 17. GDR width, centroid energy, and deformation parameter as a function of average *T* for two windows of average *J*. See Table III for the spread in *T* for each data point.

Another aspect that can be addressed from these data is the dependence of the GDR parameters on *T* for the same *J* window and vice versa over a restricted range. Figures 16 and 17 show such plots. For an average temperature of $\sim$1.3 MeV, Γ_D is almost constant for a large variation in *J*. Although each point in Fig. 16 also corresponds to a range of *J* values, the inherent *J* dependence is the same for this case. On the other hand, for the two different average angular momenta around $\sim 12\hbar$ and $23\hbar$, Γ_D increases significantly with *T* in both the cases. Thus, these measurements disentangle the effect of temperature and angular momentum and show that the GDR width increases due to the effect of *T* and not of *J*. It is interesting to compare the present observation with the earlier measurements in terms of the rotational frequency (ω_{rot}). In Sn nuclei [19], the width significantly increases over a range of $J=30$–54. This corresponds to a range of $\hbar\omega_{rot}\sim 0.8$–$1.5$ MeV. However, in these measurements there is a change of $\sim$0.4 MeV in temperature. If the effect of temperature is taken into account the exclusive dependence of Γ_D on *J* would be even stronger. In the present work the observed Γ_D is a constant over a range of average $\hbar\omega_{rot}$ from $\sim$0.4 to 1.3 MeV. (Considering the variation in *J* around each averaged *J* value, the actual range of $\hbar\omega_{rot}$ is wider than this.) For a similar change in the rotational frequencies, the width changes from $\sim$8.5 to 11.5 MeV in the Sn nuclei in marked contrast to the present results.

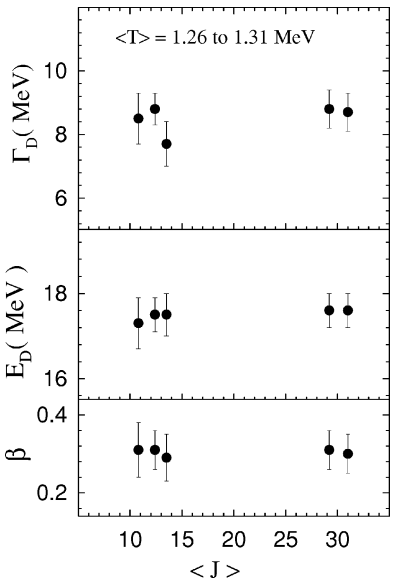

FIG. 16. GDR width, centroid energy, and deformation parameter as a function of average *J* for a restricted range of average *T*. See Table III for the spread in *J* for each data point.

Figures 16 and 17 show that the small change in the effective deformation is also caused mainly by temperature with no apparent effect from the angular momentum. Finally, a surprising observation is the apparent variation of the GDR centroid energy with average *T* as shown in Fig. 17. The centroid energy is a constant over a range of $\sim$1.2–1.6 MeV of average temperature, but shows a decrease of about 1 MeV below $\langle T\rangle\sim 1.2$ MeV. Since the decrease in the centroid energy is observed only for the higher *J* window, this could be a combined effect of both temperature and angular momentum. The decrease in E_D arises, in a phenomenological description of the GDR, from a weakening of the isovector potential or the increase in the inertial parameter describing the collective motion or both. It will be interesting to understand this observation from a microscopic calculation.

VI. SUMMARY

High-energy γ-ray spectra in the energy range of $\sim 4-35$ MeV were measured in coincidence with a γ-ray multiplicity detector array in the reaction $^{28}\mathrm{Si}+^{58}\mathrm{Ni}$ at $E(^{28}\mathrm{Si})=100$ and at 125 MeV. The compound nucleus ^{86}Mo was populated at the excitation energies of ~ 49 and 66 MeV and at angular momenta up to $30\hbar$ and $46\hbar$, respectively. These data were analyzed using the statistical model code CASCADE incorporating the GDR built on excited states. The GDR centroid energies and widths were extracted as a function of multiplicity which is related to angular momentum. The average temperature and angular momentum over various steps of GDR photon emission were calculated after making the necessary modifications in the CASCADE code. The extracted GDR width increases by ~ 4.5 MeV for a change in average temperature from 1.1 MeV to 1.6 MeV. No dependence on angular momentum is observed at an average temperature of ~ 1.3 MeV. Considering an overlapping rotational frequency region ($\hbar\omega_{rot} \sim 0.8-1.3$ MeV), the observed J independence in this work differs from that reported in the Sn region. In the latter case, the increase in width is attributed to the oblate flattening of the nuclei. In the present work, no evidence for oblate shapes is seen. The extracted strength functions can be described as due to prolate shapes with an effective deformation slightly increasing with temperature. The extracted GDR centroid energies are close to the ground state values of the nearby stable nuclei. However, there is a decrease of ~ 1 MeV below an average temperature of 1.2 MeV, when the average angular momentum is above $\sim 20\hbar$.

ACKNOWLEDGMENTS

The authors thank R.G. Pillay for his valuable help in the clover detector gated measurements and the Pelletron accelerator staff for the excellent operation of the machine during the runs. One of the authors (S.K.R.) thanks the Department of Atomic Energy, India, for providing support during this work.

[1] F.S. Dietrich, J.C. Browne, W.J. O'Connell, and M.J. Kay, Phys. Rev. C **10**, 795 (1974).
[2] J.O. Newton, B. Herskind, R.M. Diamond, E.L. Dines, J.E. Draper, K.H. Lindenberger, C. Schuck, S. Shih, and F.S. Stephens, Phys. Rev. Lett. **46**, 1383 (1981).
[3] K.A. Snover, Annu. Rev. Nucl. Part. Sci. **36**, 545 (1986).
[4] J.J. Gaardhøje, Annu. Rev. Nucl. Part. Sci. **42**, 483 (1992).
[5] P.F. Bortignon, R.A. Broglia, G.F. Bertsch, and J. Pacheco, Nucl. Phys. **A460**, 149 (1986).
[6] P. Donati, N. Giovanardi, P.F. Bortignon, and R.A. Broglia, Phys. Lett. B **383**, 15 (1996).
[7] N.D. Dang and A. Arima, Phys. Rev. Lett. **80**, 4145 (1998).
[8] M. Gallardo, M. Diebel, T. Døssing, and R.A. Broglia, Nucl. Phys. **A443**, 415 (1985).
[9] Y. Alhassid and B. Bush, Nucl. Phys. **A509**, 461 (1990).
[10] W.E. Ormand, P.F. Bortignon, R.A. Broglia, and A. Bracco, Nucl. Phys. **A614**, 217 (1997).
[11] A. Ansari, N. Dinh Dang, and A. Arima, Phys. Rev. C **63**, 024310 (2001).
[12] E. Ramakrishnan *et al.*, Phys. Rev. Lett. **76**, 2025 (1996).
[13] T. Baumann *et al.*, Nucl. Phys. **A635**, 428 (1998).
[14] A. Bracco, F. Camera, M. Mattiuzzi, B. Million, M. Pignanelli, J.J. Gaardhøje, A. Maj, T. Ramsøy, T. Tveter, and Z. Zelazny, Phys. Rev. Lett. **74**, 3748 (1995).
[15] M. Mattiuzzi, A. Bracco, F. Camera, W.E. Ormand, B. Million, M. Pignanelli, J.J. Gaardhøje, A. Maj, T. Ramsøy, and T. Tveter, Nucl. Phys. **A612**, 262 (1997).
[16] R.F. Noorman, Nucl. Phys. **A574**, 501 (1994).
[17] G. Viesti *et al.*, Nucl. Phys. **A604**, 81 (1996).
[18] M. Kmiecik, A. Maj, A. Bracco, F. Camera, M. Casanova, S. Leoni, B. Million, B. Herskind, R.A. Bark, and W.E. Ormand, Nucl. Phys. **A674**, 29 (2000).
[19] M. Mattiuzzi, A. Bracco, F. Camera, B. Million, M. Pignanelli, J.J. Gaardhøje, A. Maj, T. Ramsøy, T. Tveter, and Z. Zelazny, Phys. Lett. B **364**, 13 (1995).
[20] F. Camera *et al.*, Phys. Rev. C **60**, 014306 (1999).
[21] D.R. Chakrabarty, V.M. Datar, R.K. Choudhury, B.K. Nayak, Y.K. Agarwal, C.V.K. Baba, and M.K. Sharan, Phys. Rev. C **53**, 2739 (1996).
[22] S.D. Paul, H.C. Jain, S. Chattopadhyay, M.L. Jhingan, and J.A. Sheikh, Phys. Rev. C **51**, 2959 (1995).
[23] S.K. Rathi, S. Kumar, E.T. Mirgule, H.H. Oza, A. Mitra, V.M. Datar, and D.R. Chakrabarty, Nucl. Instrum. Methods Phys. Res. A **482**, 355 (2002).
[24] F. Puhlhofer, Nucl. Phys. **A280**, 267 (1977).
[25] W. Nelson, H. Hirayama, and D. Roger, Stanford University Report SLAC-265 1985 (unpublished).
[26] D.R. Chakrabarty, S.K. Rathi, V.M. Datar, S. Kumar, E.T. Mirgule, A. Mitra, and H.H. Oza, Nucl. Phys. **A712**, 23 (2002).
[27] A.V. Ignatyuk, G.N. Smirenkin, and A.S. Tishin, Sov. Phys. J. **21**, 255 (1975).
[28] D. Wilmore and P.E. Hodgson, Nucl. Phys. **55**, 673 (1964).
[29] F.G. Perey, Phys. Rev. **131**, 745 (1963).
[30] L. McFadden and G.R. Satchler, Nucl. Phys. **84**, 177 (1966).
[31] D.R. Chakrabarty, M. Thoennessen, N. Alamanos, P. Paul, and S. Sen, Phys. Rev. Lett. **58**, 1092 (1987).
[32] S.S. Dietrich and B.L. Berman, At. Data Nucl. Data Tables **38**, 199 (1988).
[33] M. Danos, Nucl. Phys. **5**, 23 (1958).